Applied Catalysis B: Environmental 203 (2017) 955–963

Contents lists available at ScienceDirect

Applied Catalysis B: Environmental

journal homepage: www.elsevier.com/locate/apcatb

Sequential two-step hydrothermal growth of MoS_2/CdS core-shell heterojunctions for efficient visible light-driven photocatalytic H_2 evolution

Aiping Wu [a], Chungui Tian [b], Yanqing Jiao [b], Qing Yan [b], Guoyu Yang [a,*], Honggang Fu [b,*]

[a] Key Laboratory of Cluster Science, Ministry of Education of China, Beijing Institute of Technology, Beijing 100081, China
[b] Key Laboratory of Functional Inorganic Material Chemistry, Ministry of Education of China, Heilongjiang University, Harbin 150080, China

ARTICLE INFO

Article history:
Received 23 August 2016
Received in revised form 26 October 2016
Accepted 6 November 2016
Available online 9 November 2016

Keywords:
Photocatalytic H_2 evolution
Core-shell structure
CdS
MoS_2
Visible light-driven catalyst

ABSTRACT

The visible-light driven, Pt-free photocatalytic H_2 evolution (PHE) is promising for clean and sustainable H_2 production. The construction of the heterojunction structure with intimate contact and good light adsorption ability is important for realizing the high effective PHE. Here, the core-shell structured MoS_2/CdS hybrids were constructed through "sequential two-step hydrothermal growth" route for Pt-free PHE. In the synthesis, the hierarchical flower-like MoS_2 was firstly obtained through the reaction of ammonium molybdate and excessive thiourea. Subsequently, without need of centrifugation, the cadmium acetate (Cd source) was added into the cooled MoS_2 solution directly followed by a secondary hydrothermal reaction. In the process, the Cd^{2+} could react with partially S^{2-} in MoS_2 (substituted reaction) and with the excessive S^{2-} ions in solution to generate CdS, resulting in the formation of CdS shell contacted with MoS_2 core. The micro-structure of the composites (such as the thickness and morphology of CdS shell) could be tuned by changing the amount of Mo source and Cd source. In the composites, the CdS on the outside is convenient to absorb the solar light. The intimate contact of CdS and MoS_2 is beneficial to charge transfer. As a result, the MoS_2/CdS catalyst showed high catalytic activity for PHE under visible light irradiation ($\lambda > 420$ nm). The H_2 evolution rate could reach to 775 μmol h^{-1} (20 mg catalyst), which is much higher than pure CdS (12 μmol h^{-1}) and Pt-CdS (64 μmol h^{-1}). The good activity should be related with CdS outside shell beneficial for light adsorption and intimate contact of CdS and MoS_2 for easy charge transfer. A series of experiments demonstrate that the formation of the heterojunction can effectively enhance the charge transfer ability and retard the recombination of electron-hole pairs, thus improving PHE activity and alleviating the photocorrosion of CdS component.

1. Introduction

Environmental and energy questions are faced by the people over the world. Photocatalysis driven by light energy in the presence of the semiconductors provides a promising solution to the environmental and energy problems due to their potential for the removal of toxic pollutants, the reduction of CO_2 and the production of hydrogen from water [1–3]. Most of the hydrogen is currently produced by steam-reforming of fossil fuels, with the greenhouse gas CO_2 formed as a byproduct [4]. So, the hydrogen produced by reduction of H^+ in water can be CO_2 emission-free, clean and sustainable methods for H_2 evolution [5]. Since 1972, the TiO_2-based semiconductors have become most studied catalyst for PHE [6,7]. However, the broad band-gap of TiO_2 makes them to be UV-light active with Pt as co-catalyst [8]. The black TiO_2 obtained by reduction of TiO_2 is a visible-light active catalyst, but the Pt still be needed in most case with low-quantum yields [9,10].

Many non-TiO_2 catalysts have been explored, such as C_3N_4, ZnS, titanate ($SrTiO_3$, $NiTiO_3$) and CdS [11–18]. Among them, CdS, with the relatively narrow band gap (2.4 eV) and the proper position of the conductive band (−0.52 eV), has been considered as a promising visible-light-driven catalyst. Generally, a co-catalyst should be used to inhibit the recombination of the photo-generated carriers and to provide active center for H^+ reduction [19]. Platinum (Pt) has been widely acknowledged as the most active co-catalyst for the photocatalytic H_2 evolution (PHE). Gong et al. have demonstrated that CdS cluster/graphene nanosheets loaded with Pt have shown the enhanced catalytic activity [16]. However, the high cost and scarce characteristics of Pt hinder its practical application. The replacement of Pt with low-cost co-catalyst is very promising. Since first

* Corresponding authors.
E-mail addresses: ygy@bit.edu.cn (G. Yang), fuhg@vip.sina.com (H. Fu).

http://dx.doi.org/10.1016/j.apcatb.2016.11.009
0926-3373/

identification of active sites of MoS_2 for HER [20,21], the MoS_2 with a layered crystal structure is considered as a good replacement of Pt in the catalytic fields. Dai et al. have demonstrated that MoS_2/RGO hybrids exhibited excellent HER activity [22]. Paralleled with the application in electro-catalytic filed, many works have shown that MoS_2 can also be used as non-Pt co-catalyst of TiO_2, ZnS, $ZnIn_2S_4$, CdZnS and CdS for PHE [23–32]. Li et al. have demonstrated that the activity of CdS can be greatly improved by loading MoS_2 [27]. Ye et al. have reported that the sequential grown of MoS_2 and CdS on graphene can give a ternary CdS-MoS_2/graphene catalyst that shown an enhanced H_2 evolution activity [28].

For CdS-MoS_2 system, the CdS acts as light absorber and MoS_2 as co-catalysts to provide proton reduction sites. So, in principle, the placement of CdS on outside surface of MoS_2 is beneficial to absorb the light. Meanwhile, the intimate contact of light absorber and co-catalyst is also essential for the effective charge-transfer, thus improving the photocatalytic activity. In previous reports, the CdS-MoS_2 based catalysts usually were obtained by two basic routes. One is the deposition of MoS_2 on preformed CdS rods (or particles) [27,33–36]. The other is first growth of CdS on supports (graphene), and then deposition of MoS_2 on composite support [28,37–39]. In the former route, the CdS can be (partially) coated with MoS_2, which can affect the light absorption ability of CdS. For second strategy, the CdS can also deposit on graphene besides the MoS_2 on graphene, which impede the effective contact of MoS_2 and CdS. From this point, the core-shell structured MoS_2/CdS composed with outside CdS shell and inner MoS_2 core is very suitable for photocatalytic H_2 evolution.

The ions exchange method is demonstrated to be effective for the preparation of nano-structured material, such as oxides, sulfides and selenides [40–45]. The MoS_2 contains numerous sulfur ions, so it can be a potential sulfur source for ions exchange reaction. If Mo can be partially replaced by Cd, it is very possible to generate MoS_2/CdS core-shell structure with effective contact. In this paper, based on this concept, we developed an effective "in-situ substitution and growth" method to prepare the core-shell structured MoS_2/CdS materials. The hierarchical flower-like MoS_2 was firstly prepared as a core for subsequent growth of CdS shell. The selection of the hierarchical MoS_2 is based on their larger S_{BET} and more stable structure than layer MoS_2. Subsequently, without need of centrifugation, the cadmium acetate (Cd source) was added into the cooled MoS_2 solution directly followed by a further (secondary) hydrothermal reaction. The material has the following characteristics: 1) The CdS on the outside is convenient to absorb the solar light; 2) in-situ substitution reaction is favorable to form intimate contact of MoS_2 and CdS; 3) the "one-pot" operation is relatively simple and easy to be controlled. Experimental results suggested that the as-prepared hierarchical core-shell structured MoS_2/CdS showed enhanced visible light photocatalytic H_2 evolution activity of 775 μmol h^{-1} (20 mg catalyst, about 15.5 mmol h^{-1} g^{-1}). The good activity should be related with CdS outside shell beneficial for light adsorption and intimate contact of CdS and MoS_2 for easy charge transfer.

2. Experimental section

2.1. Materials and chemicals

Polyvinylpyrrolidone (PVP), thiourea, Ammonium molybdate tetrahydrate ($H_{24}Mo_7N_6O_{24}{\cdot}4H_2O$) and cadmium acetate dihydrate ($C_4H_6O_4Cd{\cdot}2H_2O$) were all purchased from Aladdin Chemical Reagent Co., Ltd. All of the reagents were of analytical grade and used without any further purification. Deionized water was used throughout the experiments.

2.2. Synthesis of MoS_2/CdS nanomaterials

A "sequential two-step hydrothermal growth"method was developed to construct the core-shell structured MoS_2/CdS composites. The hierarchical flower-like MoS_2 was first formed by the hydrothermal reaction of ammonium molybdate and excessive thiourea [46]. In a typical synthesis, 0.35 g of $H_{24}Mo_7N_6O_{24}{\cdot}4H_2O$, 0.76 g of thiourea and 0.25 g PVP were dissolved in 40 mL of deionized water to form a clear solution. After stirring for 1 h at room temperature, the solution was transferred into a 100 mL of Teflon-lined stainless steel autoclave, sealed tightly, and heated at 473 K for 24 h. After cooling naturally to room temperature, 20 mL of cadmium acetate (0.6 M) solution was added into the autoclave containing MoS_2 solution. After stirring for 1 h at room temperature, the autoclave was sealed and heated at 453 K for 12 h. The products were collected by centrifugation, and then soaked in acetic acid for 1 h to remove impurity. Final solids were obtained by centrifugation and washing with water and ethanol, and dried at 333 K. By varying the amounts of Cd source, the composites with different ratio of MoS_2 and CdS were prepared. The samples prepared with different molar ratios of original Mo and Cd (1:1, 1:2, 1:4, 1:6, 1:8) were denoted as MoS_2/CdS-1, MoS_2/CdS-2, MoS_2/CdS-4, MoS_2/CdS-6 and MoS_2/CdS-8, respectively. In addition, The pure CdS was prepared by reaction of 2 mmol of cadmium acetate dihydrate and 10 mmol of thiourea at 453 K for 12 h.

2.3. Characterizations

Transmission electron microscopy (TEM: JEM-2100, 200 kV) and Scanning electron microscopy (SEM, Hitachi S-4800, 5 kV) were used to characterize the morphology of the samples. X-ray powder diffraction (XRD) patterns were collected on a Bruker D8 diffractometer using Cu Kα (λ = 1.5406 Å) radiation with accelerating voltage 40 kV. X-ray photoelectron spectroscopy (XPS) test was performed on VG ESCALAB MK II using an Mg Ka (1253.6 eV) achromatic X-ray radiation. Scanning Kelvin probe (SKP) test (SKP5050 system, Scotland) was used to test the work function of samples at ambient atmosphere. The gold electrode was selected as reference electrode. The specific surface area of the samples was tested on a Micromeritics Tristar II and calculated by the Brunauer–Emmett–Teller (BET) method.

2.4. Photocatalytic H_2 evolution test

The photocatalytic H_2 evolution test was carried out on an online photocatalytic hydrogen production system (AuLight, Beijing, CEL-SPH2N). A 300 W Xe lamp with a UV-cutoff filter (λ > 420 nm) was used as a visible light source to trigger the photocatalytic reaction. In a typical photocatalytic test, 20 mg of the catalysts were dispersed in a mixed solution of lactic acid (20 mL) and water (80 mL). Prior to irradiation, the system was deaerated to remove the dissolved air in order to assure anaerobic conditions in the reaction system. The evolved H_2 was analyzed using an on-line gas chromatograph (SP7800, TCD, molecular sieve 5 Å, N_2 carrier, Beijing Keruida Technology Co., Ltd). In the cycling test, the photocatalyst was separated by centrifugation and re-dispersed in the fresh mixed solution of lactic acid and water for each test. The apparent quantum efficiency (AQE) of the catalyst for H_2 evolution was measured by applying a Xe lamp (300 W) with a 420 nm band-pass filter. The AQE was calculated according to the following equation [47]:

$$\mathrm{AQE}\,(\%) = \frac{2 \times \textit{the number of evolved H2 molecules}}{\textit{the number ofincident photons}}$$

Photocurrents were measured using an electrochemical workstation (BAS 100B) in a standard three-electrode system at a 0.5 V

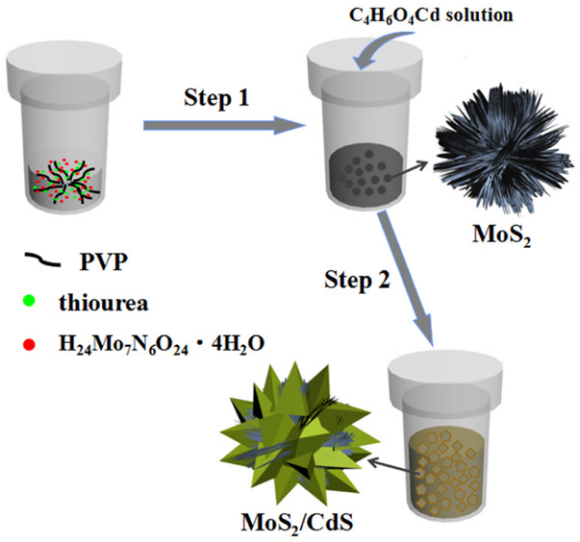

Scheme 1. Schematic for the formation of MoS_2/CdS composites.

potential bias under a 300 W Xe arc lamp with the prepared samples as the working electrodes, a Pt foil as the counter electrode, and a saturated calomel electrode (SCE) as a reference electrode. A 0.5 M Na_2SO_4 aqueous solution was used as the electrolyte. Electrochemical impedance spectroscopy (EIS) was performed in a dummy cell with a computer-controlled IM6e impedance measurement unit (Zahner Elektrik, Germany).

3. Results and discussion

3.1. The morphology and structure characterization of MoS_2/CdS

The MoS_2/CdS composites were fabricated through a "sequential two-step hydrothermal growth" route (Scheme 1). In the first-step, the MoS_2 spheres were prepared by reaction of Mo source with S^{2-} released by NH_2CSNH_2 in the presence of PVP as structure-direct reagent. After reaction, there are residual S^{2-} source in the solution because the excessive S^{2-} source was added. The presence of residual S^{2-} can be demonstrated by adding Ag^+ in supernatant obtained by centrifugation. In this case, a black precipitation (Ag_2S) is formed. After adding of the cadmium source, the Cd^{2+} ions will react with S^{2-} both in MoS_2 and in solution to form CdS. The replacement of Mo in MoS_2 by Cd is favorable to generate heterojunction MoS_2/CdS with good interfacial contact. The crystal structure of the MoS_2 from first-step hydrothermal reaction is analyzed by XRD method. The diffraction peaks located at $2\theta = 13^\circ$, 33° and 59° can be assigned to (002), (100) and (110) planes of MoS_2 (JCPDS 37-1492) respectively. The microstrucutre of the MoS_2 was studied by SEM and TEM. From the SEM images (Fig. S1a), we can see that the size of the MoS_2 sphere is about 180 nm with good uniformity. The TEM images (Fig. 1b, Fig. S1) show the formation of the flower-like MoS_2 nanosphere. A closer examination with TEM indicates that the MoS_2 nanospheres are composed of sheet-like sub-units to form relatively loose spheres (Fig. S1c–d).

In second hydrothermal process, the amount of residual S^{2-} ions in solution is lack in relative to the Cd^{2+} ions. So, a part of S^{2-} in MoS_2 should act as S^{2-} source reacting with Cd^{2+}. The solids separated from secondary hydrothermal reaction are tested by XRD method (molar ratio of Mo/Cd is 1:6). The peaks belonging to $CdMoO_4$ and $CdCO_3$ can be observed, besides CdS and MoS_2 as shown in Fig. S2. The CO_3^{2-} ions should be from hydrolysis of thiourea and the MoO_4^{2-} should be mainly from the ammonium molybdate that act as Mo source in the synthesis. Therefore, the excessive Cd^{2+} can react with CO_3^{2-} and MoO_4^{2-} to form $CdCO_3$ and $CdMoO_4$. For CdS-based catalyst, the activity is usually evaluated in acid medium. So, the solids were immersed in acetic acid (or lactic acid) to remove acid-soluble components ($CdCO_3$, $CdMoO_4$). After treatment, the XRD pattern indicates the presence of the CdS and MoS_2 phases, and no other peaks are observed, indicating the effective removement of $CdMoO_4$ and $CdCO_3$ (Fig. 1a).

Fig. 1c–g represents the TEM and high-resolution TEM (HRTEM) images of the MoS_2/CdS-6 sample. The size of the MoS_2/CdS-6 is about 250 nm which is slightly larger than MoS_2 sphere from first-step reaction (Fig. 1c). Being different with MoS_2, the polyhedrons with sharply tip can be seen on the outside surface of the MoS_2/CdS-6. The high-resolution TEM images (HRTEM, Fig. 1d–g) show that the interlayer distance of polyhedrons is about 0.33 nm, which can be indexed to the (002) plane of hexagonal CdS. In addition, the (002) plane of MoS_2 with interlayer distance 0.64 nm can also be observed. From TEM, we can observe the intimately contact between CdS and MoS_2 components, which should be favorable to the electron transfer between two phases. In addition, the CdS are located on the outside surface, which is desirable for effective adsorption of light. The pores from the accumulation of CdS can be observed. The porous structure can provide the highly accessible interface for easy transferring of the reagents and migrating of the photo-generated electrons. In addition, SEM images (Fig. S3) show that the CdS with sharply tip are grown on the MoS_2 to form MoS_2/CdS core shell structure.

In order to investigate the chemical composition and valence state of the MoS_2/CdS sample, the X-ray photoelectron spectroscopy (XPS) was performed. The XPS spectrum shows the co-consistence of Mo, Cd and S elements in the MoS_2/CdS-6 sample (Fig. 2a). Fig. 2b shows the high resolution XPS spectrum of Cd 3d region. Two peaks at 411.4 and 404.6 eV are attributed to Cd $3d_{3/2}$ and $3d_{5/2}$ of Cd^{2+} in CdS. From Fig. 2c we can see that the Mo 3d spectrum of MoS_2 shows the doublet with Mo (+4) $3d_{3/2}$ binding energy at 232.45 eV and Mo (+4) $3d_{5/2}$ binding energy at 229.35 eV. For MoS_2/CdS-6, the binding energy of Mo (+4) 3d loads at 231.95 eV ($3d_{3/2}$) and 228.85 eV ($3d_{5/2}$). A negative-shift of 0.5 eV can be seen by comparison with pure MoS_2. We know that the XPS is surface-sensitive technique that can be used to analyze the surface elements of the materials, and it is difficult to detect the elements in core components of a core-shell structure with a *dense and thick shell. In the MoS_2/CdS, the detection of the* Mo from MoS_2 should be ascribed to the uncomplete coverage of CdS on MoS_2. Thus the X-ray can reach to the MoS_2 and the Mo 3d peaks can be observed. To further demonstrate the transfer, the XPS spectrum of Cd is also analyzed. For pure CdS, the Cd $3d_{5/2}$ and $3d_{3/2}$ peaks are located at 403.7 eV and 410.5 eV, respectively (Fig. S4c–d). After compounding with MoS_2, the Cd 3d peaks can be observed at 404.6 ($3d_{5/2}$) and 411.4 ($3d_{3/2}$) eV. A positive shift of 0.9 eV is obviously seen in comparison with pure CdS. The result is attributed to the electron transfer from CdS to MoS_2. Such a transfer is very favorable to improve the performance of catalyst. Fig. 2d shows the high resolution XPS spectrum of S 2p region. For MoS_2, the S $2p_{1/2}$ and $2p_{3/2}$ peaks are located at 163.35 and 162.15 eV, being consistent with the reported values of S2p for MoS_2. For MoS_2/CdS-6, the peaks locate at 162.25 and 161.15 eV. The O 1s peaks (Fig. S4a–b) can be deconvoluted into three peaks, corresponding to the surface-adsorbed oxygen species, the oxygen of surface hydroxyl and the lattice oxygen. The XPS results further confirm the formation of MoS_2/CdS composites, especially, the presence of strong interaction between CdS and MoS_2. The ESR test also indicates the presence of interaction and electron transfer from CdS to MoS_2 (Fig. S5), being consistent with that of the XPS.

The ratio of different components in composites is important for regulating their properties and application performance. In present

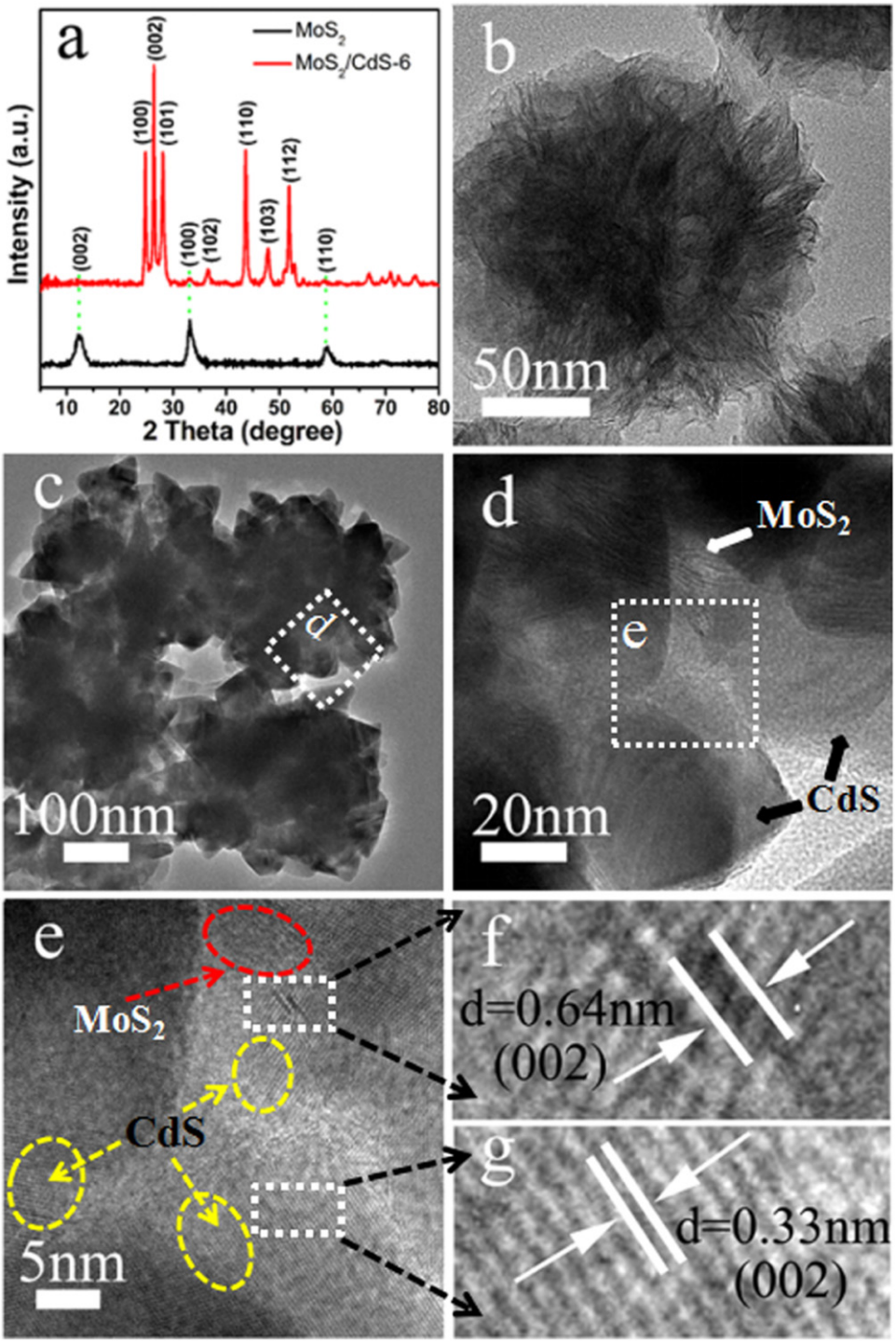

Fig. 1. a) XRD patterns and TEM images of b) MoS_2 spheres and c-g) MoS_2/CdS-6.

synthesis, the ratio of CdS and MoS_2 can be easily tuned by changing the amount of Cd source added in secondary hydrothermal process. The samples with different molar ratios of Mo and Cd (1:1, 1:2, 1:4, 1:8) are synthesized under the same conditions with the synthesis of the MoS_2/CdS-6, which are denoted as MoS_2/CdS-1, MoS_2/CdS-2, MoS_2/CdS-4 and MoS_2/CdS-8. Fig. 3 shows the XRD patterns of different MoS_2/CdS samples. For all samples, the peaks corresponding to MoS_2 and CdS can be observed. The diffraction peaks located at 2θ = 13°, 33° and 59° are assigned to (002), (100) and (110) planes of MoS_2. The peaks locate at 2θ = 24.9°, 26.5°, 28.2°, 43.8°, 47.8°, 51.9° are indexed to (100), (002), (101), (110), (103) and (112) plane of hexagonal CdS. We can see that the peak intensity of CdS is in the order of MoS_2/CdS–8 > MoS_2/CdS–4 > MoS_2/CdS–2 > MoS_2/CdS-1. For MoS_2/CdS-1, only weak peaks of CdS phase can be seen, but it gives strong CdS peaks for MoS_2/CdS-8 sample. Meanwhile, as shown in Fig. 3, both the cubic phase and hexagonal phase CdS can be observed for MoS_2/CdS-1 and MoS_2/CdS-2 samples. The intensity of cubic phase CdS decreases gradually with the increase of the ratio of Cd^{2+}. For MoS_2/CdS-4, the peaks corresponding to the cubic phase CdS are not obvious and it is undetectable for MoS_2/CdS-6 sample. In addition, for samples with high ratio of CdS, the diffraction peak of (002) plane of MoS_2 became weaker and finally almost

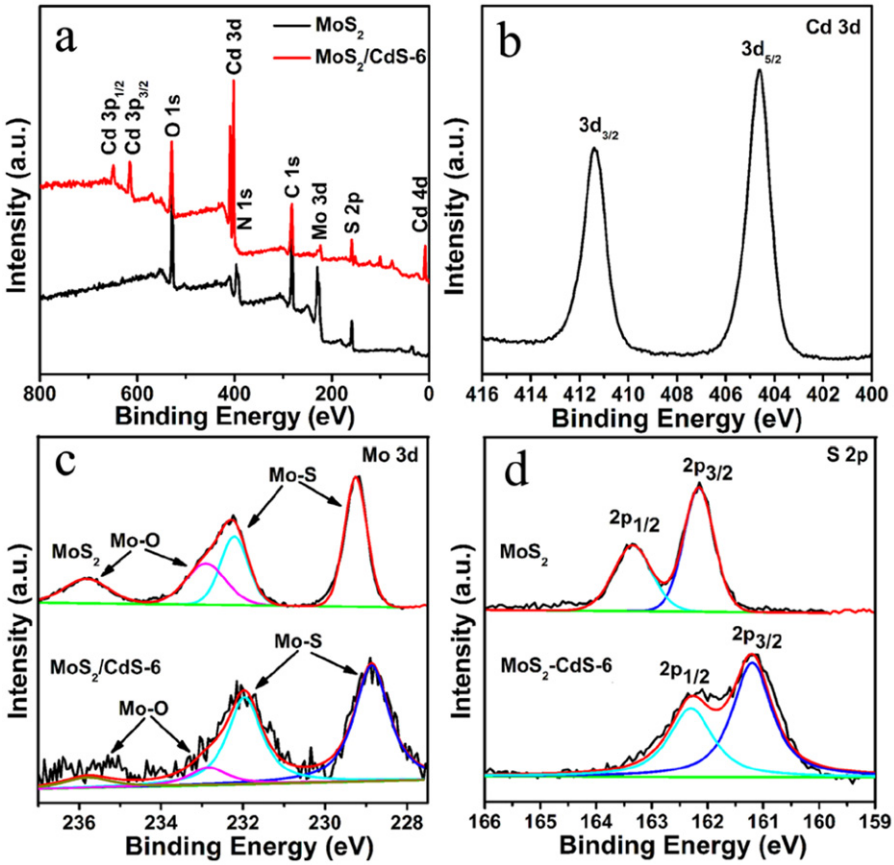

Fig. 2. XPS of MoS_2 and MoS_2/CdS-6: a) survey spectrum, b) Cd 3d spectrum, c) Mo 3d spectrum and d) S 2p spectrum.

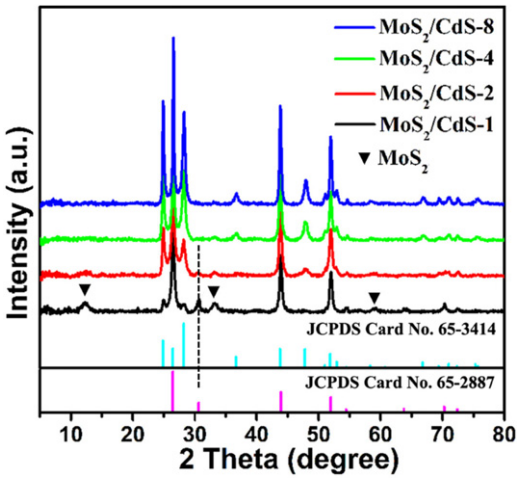

Fig. 3. XRD patterns of MoS_2/CdS nanocomposites.

disappeared, but the diffraction peaks of (100) and (110) planes can be still observed. The absence of the (002) diffraction peak indicates the few-layer characteristics of MoS_2 nanosheets in the MoS_2/CdS composites.

The structure of the different samples is studied by TEM and SEM methods (Fig. 4, Fig. S6–S8). Fig. S7 (a–c) and Fig. S8 (a, b) show the TEM and SEM images of MoS_2/CdS-1 sample. It can be seen that CdS particles with irregular shape are grown on the MoS_2 as the low amount of Cd source is added. When the molar ratio of Cd and Mo is increased to 2, the CdS nanoparticles uniformly covered on the MoS_2 surface with higher density than that in MoS_2/CdS-1 sample (Fig. 4a–c and Fig. S6a–b). For MoS_2/CdS-4 (Fig. S7d–f and Fig. S8c–d), the size of CdS particles increases in company with a further increase of the cover degree. In addition, a part of CdS shows the polyhedral shape besides the irregular particles that are majority in MoS_2/CdS-1 and MoS_2/CdS-2 samples. For MoS_2/CdS-6, the percentage of polyhedral CdS is further increased (Fig. 1c–d). At high ratio of Cd/Mo (8:1), the polyhedral CdS particles with size about 50 nm are uniformly grown on the surface. The MoS_2 cannot be observed on the surface of MoS_2/CdS-8 sample (Fig. 4d–f, Fig. S6c–d). ICP test was also performed to determine the proportion of Mo and Cd. The corresponding results were shown in Table S1. It can be seen that the Mo/Cd ratios are about 0.836, 0.281, 0.176, 0.142 and 0.117 for MoS_2/CdS-1, MoS_2/CdS-2, MoS_2/CdS-4, MoS_2/CdS-6 and MoS_2/CdS-8, respectively. The Mo/Cd also gradually decreases with the increase of the amount of Cd source. Above results verify that the ratio of MoS_2/CdS and the morphology of CdS can be tuned easily by changing the amount of the Cd source.

3.2. *Visible light-driven photocatalytic H_2 evolution*

The visible-light driven, Pt-free photocatalytic H_2 evolution is promising for clean and sustainable H_2 production. For effective visible light, the catalyst should be visible-light responsible. UV–vis diffuse reflectance spectroscopy (DRS) is used to characterize the optical properties of CdS, MoS_2 and the MoS_2/CdS-6 sample (Fig. 5a). We can see that MoS_2 has a wide absorption in the visible light region and close to the total absorption because of its narrow band gap and deep color. For CdS, the absorption at wavelengths <550 nm can be assigned to its intrinsic bandgap absorption. Compared with the pure CdS, it is very obvious that the light harvesting efficiency of MoS_2/CdS-6 is enhanced in the visible

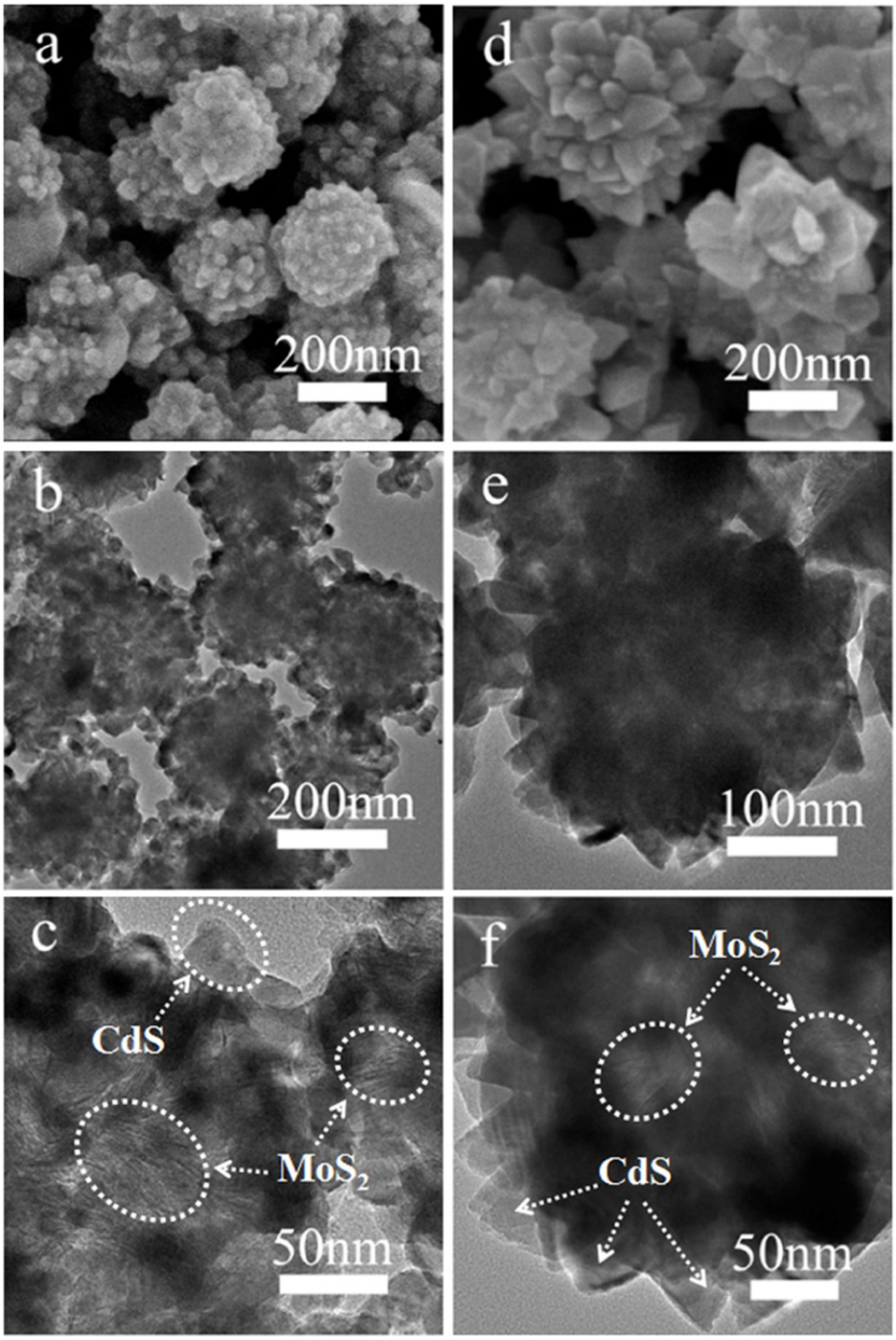

Fig. 4. SEM and TEM images of MoS_2/CdS-2 (a, b, c) and MoS_2/CdS-8 (d, e, f).

light region, which shows the enhanced absorption in the region of 500–700 nm. The enhanced light absorption of MoS_2/CdS-6 is favorable to produce more photo-generated electrons and holes, which means that more photo-generated electrons can participate in the reaction. The efficiency for the trapping and recombination of the photo-generated carriers can be verified by the photoluminescence (PL) spectroscopy. Fig. 5b shows the typical PL spectra of the CdS and MoS_2/CdS-6 under the same conditions. The MoS_2/CdS-6 exhibits much weaker emission intensity from 450 to 600 nm than pure CdS under same excitation wavelength of 350 nm. This result implies that the effective charge migrates between MoS_2 and CdS under illumination, thus indicates the lower probability in the recombination of the photogenerated electrons and holes for MoS_2/CdS than CdS. The transfer of electrons between MoS_2 and CdS is conducive to inhibit the recombination of the photogenerated charge carriers, thus enhance the photo-catalytic activity and stability of MoS_2/CdS composites.

The activities of the MoS_2/CdS for PHE are evaluated under visible-light ($\lambda > 420$ nm) irradiation using lactic acid as the hole scavenger. The results are shown in Fig. 7a. The H_2 evolution rate is about 226, 358, 574, 775, 643, 12 and 64 $\mu mol\ h^{-1}$ for MoS_2/CdS-1, MoS_2/CdS-2, MoS_2/CdS-4, MoS_2/CdS-6, MoS_2/CdS-8, CdS and Pt-

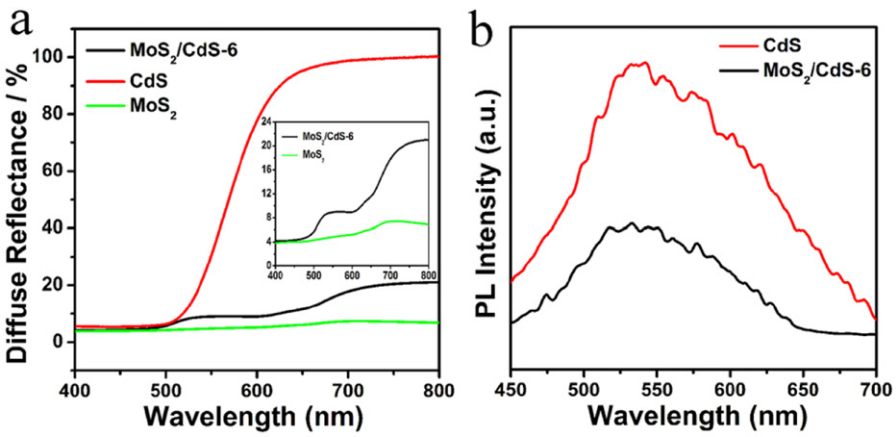

Fig. 5. UV–vis diffuses reflectance spectroscopy and PL spectra of pure CdS and MoS_2/CdS-6.

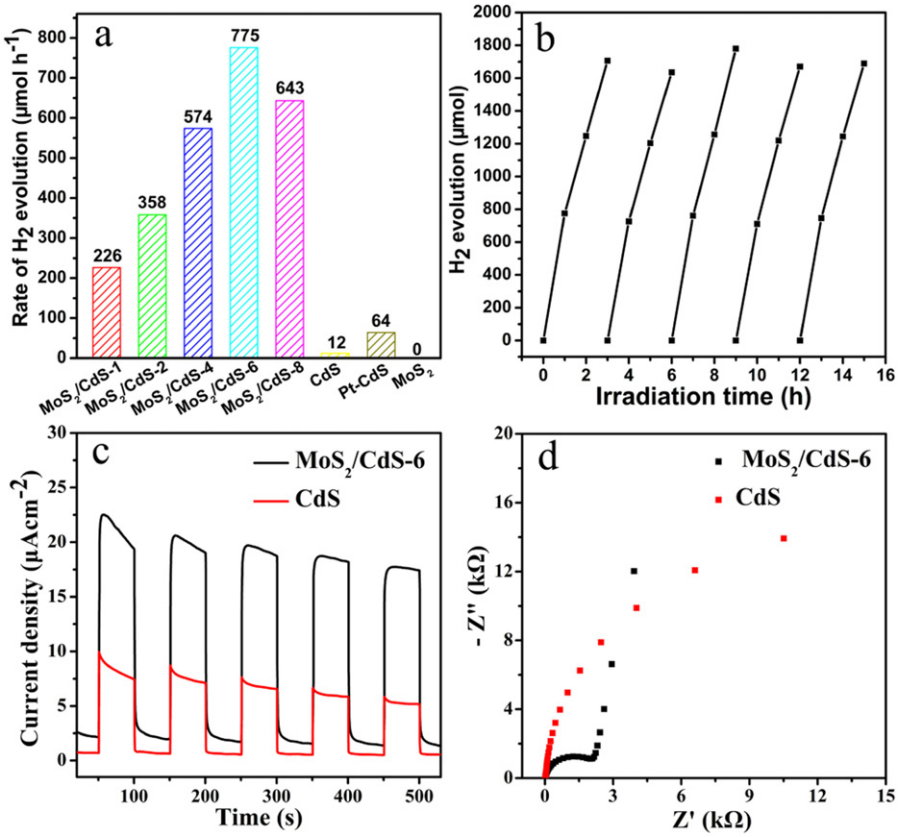

Fig. 6. a) The PHE activity of different samples; b) Cycling test of PHE activity of MoS_2/CdS-6; c) I-t curves and d) EIS Nyquist plots of CdS and MoS_2/CdS-6 in 0.5 M Na_2SO_4 solution.

CdS, respectively. It can be seen that the pure CdS shows lowest photocatalytic H_2 evolution activity. Notably, the photocatalytic activity of the MoS_2/CdS composites is remarkably enhanced after introduce of MoS_2 cocatalyst. Meanwhile, it also can be seen that blank MoS_2 has no obvious PHE activity, indicating the co-catalyst role of MoS_2. The rate of hydrogen evolution over MoS_2/CdS samples increases with increasing the molar ratios of Mo and Cd and the optimal photocatalytic activity was achieved at Mo:Cd = 1:6. The corresponding hydrogen evolution rate reached to 775 μmol h^{-1}, with an apparent quantum efficiency (AQE) of 14.7% at 420 nm. However, further increase of the molar ratios of Cd and Mo to 8:1 leads to a reduction of the photocatalytic activity. From the above SEM, TEM, XRD and ICP tests of MoS_2/CdS, it can be seen that there are little CdS grown on the MoS_2 surface in MoS_2/CdS-1, which limit the light absorption of the catalyst thus lead to the low photocatalytic activity of MoS_2/CdS-1. With increasing the content of CdS, the light absorption ability of MoS_2/CdS samples increases with the decrease of MoS_2 co-catalyst amount. In the case of proper ratio of MoS_2/CdS, the photo-generated electrons of CdS after light irradiation can be effectively trapped by MoS_2 co-catalyst for H^+ reduction. However, in the case of high ratio of CdS, the excessive CdS covered on the surface of MoS_2. Thus, the photo-generated electrons of CdS cannot be effectively trapped and utilized because the low amount of MoS_2 may hinder the transferring of electrons between MoS_2 and CdS. Therefore, the MoS_2/CdS catalysts show high PHE activity only in the case of proper ratio of MoS_2/CdS. Also, it can be seen

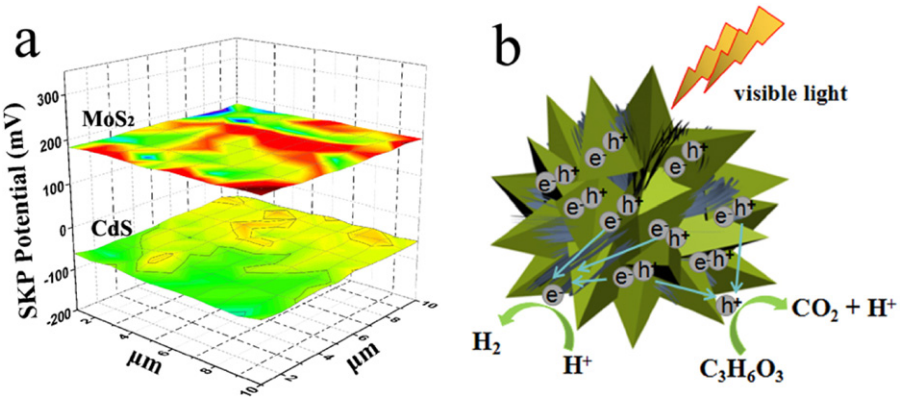

Fig. 7. a) Work function drawings of MoS_2 and CdS; b) Schematic illustration of the photocatalytic process of MoS_2/CdS composites in the lactic acid solution.

that the MoS_2/CdS-1 and MoS_2/CdS-2 samples have mixed phase CdS structure (the cubic phase and hexagonal phase CdS) shown the low PHE activity. The MoS_2/CdS-6 with undetectable cubic CdS phase possesses the best activity for PHE. The results indicate that the mixed phase is not predominant factor for high PHE activity of MoS_2/CdS sample. The formation of effective heterojunction is key to enhance the photocatalytic activity of the materials.

The noble metal (Pt, Pd, Au etc.) are well-known co-catalyst that act as electron sinks and provide effective proton reductions sites for PHE. For comparison, the Pt loaded CdS sample is also prepared by a photo-reduction method using $H_2PtCl_6{\cdot}6H_2O$ as Pt source. Under visible light irradiation, CdS sample loaded with 1 wt% Pt could significantly enhance the photocatalytic activity (64 μmol h^{-1}), while the H_2 evolution rate is still much lower than MoS_2/CdS samples. Furthermore, in order to evaluate the stability of the MoS_2/CdS-6, five consecutive photocatalytic H_2 evolution reactions were performed and each reaction was carried out under visible light irritation for 3 h. Fig. 6b shows the H_2 evolution performance in a cycling photocatalytic test. As can be seen, the amount of generated hydrogen increased steadily with the irradiation time in each cycle. In addition, after five recycles, the catalyst MoS_2/CdS-6 did not show obvious loss of activity, indicating the good photostability of the catalyst during photocatalytic H_2 evolution.

3.3. Mechanism about the enhanced PHE activity

The photocatalytic activity is closely related to the light absorption ability, specific surface area and photo-generated charge carrier separation efficiency of the photocatalyst. As discussed above, the introduction of MoS_2 has large effect on the light absorption of the samples and it is obviously seen that the light harvesting efficiency of the MoS_2/CdS was higher than the pure CdS in the visible light region. Fig. 6c shows the I-t curve of CdS and MoS_2/CdS-6 sample to analyze the effect of MoS_2 on the visible light response. It can be obviously seen that MoS_2/CdS-6 sample exhibits higher photocurrent density than pure CdS. This can be attributed to the formation of intimate contacts between MoS_2 and CdS, which significantly reduces the recombination rate of photo-generated electrons and holes. The efficient charge transfer is further verified by electrochemical impedance spectra (EIS) (Fig. 6d). The EIS Nyquist plots reveal that MoS_2/CdS-6 sample owns smaller semicircle than pure CdS, reflecting the enhanced separation and transfer efficiency of photon-generated carrier after the formation of MoS_2-CdS junctions. The specific surface area is also an important factor that affects the activity of the MoS_2/CdS samples. The nitrogen adsorption−desorption isotherms and S_{BET} values are shown in Fig. S9 and table S2. The MoS_2/CdS-6 sample shows high S_{BET} value, which is beneficial to transfer the reagent in the catalyst thus give the high PHE activity. The normalized specific area activity is about 9.93, 10.50, 26.34, 41.95 and 39.44 μmol $g\,h^{-1}\,m^{-2}$ for MoS_2/CdS-1, MoS_2/CdS-2, MoS_2/CdS-4, MoS_2/CdS-6 and MoS_2/CdS-8, respectively. It can be seen that MoS_2/CdS-6 sample has also exhibited a highest normalized specific area activity for PHE. The enhanced photocatalytic activities of MoS_2/CdS may be mainly attributed to the heterojunction between MoS_2 and CdS, which can greatly accelerate the separation of photogenerated carriers.

The work function is a fundamental property of solid surfaces that governs electron transfer and chemical reaction at the surface. The Scanning Kelvin Probe (SKP) technique was used to test the work function of MoS_2 and CdS (Fig. 7a). The work function values of MoS_2 and CdS are 5.52 and 5.28 eV, respectively. The high work function of MoS_2 indicates that the electrons on CdS photocatalyst are easy to be transferred to the MoS_2 cocatalyst, thus effective reducing the recombination of photo-generated electrons and holes, which is favorable to react of electron with H^+ to form H_2. Fig. 7b schematically illustrates the photocatalytic process of MoS_2/CdS samples. Under the irradiation of visible light, the electron–hole pairs can be generated in CdS. The electrons transfer from CdS to MoS_2 due to the high work function of MoS_2 and effective contact of MoS_2 and CdS. Finally, the electrons trapped by MoS_2 can react with adsorbed H^+ to produce H_2 due to the like-Pt activity of MoS_2.

4. Conclusions

A "sequential two-step hydrothermal growth" strategy was demonstrated to be effective to construct the MoS_2/CdS core-shell heterojunctions. The replacement of Mo in MoS_2 with Cd^{2+} is important to form the heterojunctions with the intimate interfacial contact. The microstructure could be tuned by changing the ratio of Mo and Cd source. In the composites, the exposure of the CdS out-shell is favorable to effectively utilize the light. The intimate contact of MoS_2 and CdS was favorable for the transfer and subsequent reaction of the electron. The MoS_2/CdS photocatalyst showed high catalytic activity for PHE under visible light irradiation ($\lambda > 420$ nm). The H_2 evolution rate could reach to 775 μmol h^{-1} (20 mg catalyst) with good stability. This kind of MoS_2/CdS photocatalyststs have great potential for photocatalytic H_2 evolution under visible light irradiation.

Acknowledgements

We gratefully acknowledge the support of this research by the National Natural Science Foundation of China (21371053, 21601055, 21571054), Application Technology Research and Development Projects in Harbin (2013AE4BW051), Interna-

tional Science & Technology Cooperation Program of China (2014DFR41110), Heilongjiang University Excellent Youth Foundation.

Appendix A. Supplementary data

Supplementary data associated with this article can be found, in the online version, at http://dx.doi.org/10.1016/j.apcatb.2016.11.009.

References

[1] C.C. Chen, W.H. Ma, J.C. Zhao, Chem. Soc. Rev. 39 (2010) 4206–4219.
[2] N. 2S. Habisreutinger, L.S. Mende, J.K. Stolarczyk, Angew. Chem. Int. Ed. 52 (2013) 7372–7408.
[3] X.B. Chen, S.H. Shen, L.J. Guo, S.S. Mao, Chem. Rev. 110 (2010) 6503–6570.
[4] R.M. Navarro, M.A. Peña, J.L.G. Fierro, Chem. Rev. 107 (2007) 3952–3991.
[5] X.X. Zou, Y. Zhang, Chem. Soc. Rev. 44 (2015) 5148–5180.
[6] A. Fujishima, Nature 238 (1972) 37–38.
[7] X.N. Wang, R. Long, D. Liu, D. Yang, C.M. Wang, Y.J. Xiong, Nano Energy 24 (2016) 87–93.
[8] H.Y. Li, H.W. Yu, L. Sun, J.L. Zhai, X.R. Han, Nanoscale 7 (2015) 1610–1615.
[9] Y.H. Hu, Angew. Chem. Int. Ed. 51 (2012) 12410–12412.
[10] W. Zhou, W. Li, J.Q. Wang, Y. Qu, Y. Yang, Y. Xie, K.F. Zhang, L. Wang, H.G. Fu, D.Y. Zhao, J. Am. Chem. Soc. 136 (2014) 9280–9283.
[11] J.R. Ran, T.Y. Ma, G.P. Gao, X.W. Du, S.Z. Qiao, Energy Environ. Sci. 8 (2015) 3708–3717.
[12] M. Zhang, W.J. Jiang, D. Liu, J. Wang, Y.F. Liu, Y.Y. Zhu, Y.F. Zhu, Appl. Catal. B: Environ. 183 (2016) 263–268.
[13] A.P. Wu, L.Q. Jing, J.Q. Wang, Y. Qu, Y. Xie, B.J. Jiang, C.G. Tian, H.G. Fu, Sci. Rep. 5 (2015) 8858.
[14] S.X. Ouyang, H. Tong, N. Umezawa, J.Y. Cao, P. Li, Y.P. Bi, Y.J. Zhang, J.H. Ye, J. Am. Chem. Soc. 134 (2012) 1974–1977.
[15] Y. Qu, W. Zhou, Z.Y. Ren, S.C. Du, X.Y. Meng, G.H. Tian, K. Pan, G.F. Wang, H.G. Fu, J. Mater. Chem. 22 (2012) 16471–16476.
[16] Q. Li, B.D. Guo, J.G. Yu, J.R. Ran, B.H. Zhang, H.J. Yan, J.R. Gong, J. Am. Chem. Soc. 133 (2011) 10878–10884.
[17] X.L. Zheng, J.P. Song, T. Ling, Z.P. Hu, P.F. Yin, K. Davey, X.W. Du, S.Z. Qiao, Adv. Mater. 28 (2016) 4935–4942.
[18] Y.Y. Zhong, G. Zhao, F.K. Ma, Y.Z. Wu, X.P. Hao, Appl. Catal. B: Environ. 199 (2016) 466–472.
[19] J.H. Yang, D.G. Wang, H.X. Han, C. Li, Acc. Chem. Res. 46 (2013) 1900–1909.
[20] T.F. Jaramillo, K.P. Jørgensen, J. Bonde, J.H. Nielsen, S. Horch, I. Chorkendorff, Science 317 (2007) 100–102.
[21] J. Kibsgaard, Z.B. Chen, B.N. Reinecke, T.F. Jaramillo, Nat. Mater. 11 (2012) 63–969.
[22] Y.G. Li, H.L. Wang, L.M. Xie, Y.Y. Liang, G.S. Hong, H.J. Dai, J. Am. Chem. Soc. 133 (2011) 7296–7299.
[23] Q.J. Xiang, J.G. Yu, M. Jaroniec, J. Am. Chem. Soc. 134 (2012) 6575–6578.
[24] B.L. Zhu, B.Z. Lin, Y. Zhou, P. Sun, Q.R. Yao, Y.L. Chen, B.F. Gao, J. Mater. Chem. A 2 (2014) 3819–3827.
[25] L. Wei, Y.J. Chen, Y.P. Lin, H.S. Wu, R.S. Yuan, Z.H. Li, Appl. Catal. B: Environ. 144 (2014) 521–527.
[26] S.J. Zhao, J.J. Huang, Q.Y. Huo, X.Z. Zhou, W.X. Tu, J. Mater. Chem. A 4 (2016) 193–199.
[27] X. Zong, H.J. Yan, G.P. Wu, G.J. Ma, F.Y. Wen, L. Wang, C. Li, J. Am. Chem. Soc. 130 (2008) 7176–7177.
[28] K. Chang, Z.W. Mei, T. Wang, Q. Kang, S.X. Ouyang, J.H. Ye, ACS Nano 8 (2014) 7078–7087.
[29] J.Z. Chen, X.J. Wu, L.S. Yin, B. Li, X. Hong, Z.X. Fan, B. Chen, C. Xue, H. Zhang, Angew. Chem. Int. Ed. 54 (2015) 1210–1214.
[30] K. Chang, M. Li, T. Wang, S.X. Ouyang, P. Li, L.Q. Liu, J.H. Ye, Adv. Energy Mater. 5 (2015) 1402279.
[31] X.L. Yu, R.F. Du, B.Y. Li, Y.H. Zhang, H.J. Liu, J.H. Qu, X.Q. An, Appl. Catal. B: Environ. 182 (2016) 504–512.
[32] W.J. Jiang, Y.F. Liu, R.L. Zong, Z.P. Li, W.Q. Yao, Y.F. Zhu, J. Mater. Chem. A 3 (2015) 18406–18412.
[33] X. Zong, G.P. Wu, H.J. Yan, G.J. Ma, J.Y. Shi, F.Y. Wen, L. Wang, C. Li, J. Phys. Chem. C 114 (2010) 1963–1968.
[34] Y. Liu, Y.X. Yu, W.D. Zhang, J. Phys. Chem. C 117 (2013) 12949–12957.
[35] X.Z. Zhou, J.J. Huang, H.Z. Zhang, H. Sun, W.X. Tu, Int. J. Hydrogen Energy 41 (2016) 14758–14767.
[36] X.L. Yin, L.L. Li, W.J. Jiang, Y. Zhang, X. Zhang, L.J. Wan, J.S. Hu, ACS Appl. Mater. Interfaces 8 (2016) 15258–15266.
[37] Y.X. Li, H. Wang, S.Q. Peng, J. Phys. Chem. C 118 (2014) 19842–19848.
[38] M.Q. Yang, C. Han, Y.J. Xu, J. Phys. Chem. C 119 (2015) 27234–27246.
[39] W.C. Peng, Y. Chen, X.Y. Li, J. Hazard. Mater. 309 (2016) 173–179.
[40] L.D. Trizio, L. Manna, Chem. Rev. 116 (18) (2016) 10852–10887.
[41] J.G. Yu, J. Zhang, S.W. Liu, J. Phys. Chem. C 114 (2010) 13642–13649.
[42] Y.X. Wang, Y.V. Morozov, M. Zhukovskyi, R. Chatterjee, S. Draguta, P. Tongying, B. Bryant, S. Rouvimov, M. Kuno, ACS Energy Lett. 1 (2016) 175–181.
[43] W.D. Shi, J.Q. Shi, S. Yu, P. Liu, Appl. Catal. B: Environ. 138–139 (2013) 184–190.
[44] V. Lesnyak, R. Brescia, G.C. Messina, L. Manna, J. Am. Chem. Soc. 137 (2015) 9315–9323.
[45] Q.A. Akkerman, A. Genovese, C. George, M. Prato, I. Moreels, A. Casu, S. Marras, A. Curcio, A. Scarpellini, T. Pellegrino, L. Manna, V. Lesnyak, ACS Nano 9 (2015) 521–531.
[46] A.P. Wu, C.G. Tian, H.J. Yan, Y.Q. Jiao, Q. Yan, G.Y. Yang, H.G. Fu, Nanoscale 8 (2016) 11052–11059.
[47] J. Liu, Y. Liu, N.Y. Liu, Y.Z. Han, X. Zhang, H. Huang, Y. Lifshitz, S.T. Lee, J. Zhong, Z.H. Kang, Science 347 (2015) 970–974.